

# Constraining the composition and thermal state of the moon from an inversion of electromagnetic lunar day-side transfer functions

A. Khan <sup>a,\*</sup>, J.A.D. Connolly <sup>b</sup>, N. Olsen <sup>c</sup>, K. Mosegaard <sup>a</sup>

<sup>a</sup> Niels Bohr Institute, University of Copenhagen, Denmark

<sup>b</sup> Earth Sciences Department, Swiss Federal Institute of Technology, Zurich, Switzerland

<sup>c</sup> Danish National Space Centre, Copenhagen, Denmark

Received 17 November 2005; received in revised form 6 March 2006; accepted 6 April 2006

Available online 27 June 2006

Editor: V. Courtillot

## Abstract

We present a general method to constrain planetary composition and thermal state from an inversion of long-period electromagnetic sounding data. As an example of our approach, we reexamine the problem of inverting lunar day-side transfer functions to constrain the internal structure of the Moon. We go beyond the conventional approach by inverting directly for chemical composition and thermal state, using the model system CaO–FeO–MgO–Al<sub>2</sub>O<sub>3</sub>–SiO<sub>2</sub>, rather than subsurface electrical conductivity structure, which is only an indirect means of estimating the former parameters. Using Gibbs free energy minimisation, we calculate the stable mineral phases, their modes and densities. The mineral modes are combined with laboratory electrical conductivity measurements to estimate the bulk lunar electrical conductivity structure from which transfer functions are calculated. To further constrain the radial density profile in the inversion we also consider lunar mass and moment of inertia. The joint inversion of electromagnetic sounding and gravity data for lunar composition and selenotherm as posited here is found to be feasible, although uncertainties in the forward modeling of bulk conductivity have the potential to significantly influence the inversion results. In order to improve future inferences about lunar composition and thermal state, more electrical conductivity measurements are needed especially for minerals appropriate to the Moon, such as pyrope and almandine.

© 2006 Elsevier B.V. All rights reserved.

*Keywords:* planetary composition; thermal state; inverse problems; Moon; thermodynamic modeling

## 1. Introduction

Constraining the present-day lunar thermal state is important as it holds the potential of providing valuable information on lunar origin and evolution. Moreover, temperature is a fundamental parameter in understanding the dynamic behaviour of the properties mantle in

that it governs such as viscosity, density, convection, melting and electrical conductivity. However, there are presently few data available that directly constrain lunar thermal state and most of these provide only indirect constraints. Several theoretically predicted selenotherms have been disseminated over the years (e.g. [1–5]) and show considerable scatter. These variations are mainly due to the different prior assumptions that are a prerequisite of thermal modeling, including differences in assumptions about the initial thermal state, model parameters (thermal conductivity), melting conditions

\* Corresponding author. Tel.: +45 35320564.

E-mail address: [amir@gfy.ku.dk](mailto:amir@gfy.ku.dk) (A. Khan).

and not least the relevance of subsolidus convective heat transport throughout lunar history.

Geophysical data that bear directly on the lunar temperature profile are scanty and include surface heat flow measurements [6], seismic  $Q$ -values inferred from the Apollo lunar seismic data [7] and maintenance of mascon anisotasy over a period of 3–4 b.y. [8].

A method that, in principle, can be used to put limits on the present-day lunar temperature profile involves the use of electromagnetic sounding data, which, when inverted provide knowledge on the conductivity profile of the lunar interior (e.g. [9–12]). As mineral conductivity measured in the laboratory has been found to depend inversely on temperature, limits on the selenotherm can be derived from the inferred bounds on the lunar electrical conductivity profile when combined with laboratory measurements of electrical conductivity as a function of temperature. Attempts along these lines have been undertaken (e.g. [13–17]), but were limited because of, among other things, uncertainty in bulk lunar composition and inverted electrical conductivity structure.

Building upon earlier as well as recent laboratory measurements of mineral electrical conductivities (e.g. [18–22]) our intent here is to invert measurements of the lunar inductive response to time-varying external magnetic fields during intervals when the Moon was in the solar wind or terrestrial magnetosheath in order to constrain the lunar thermal state and bulk chemical composition. Given the Moon's temperature profile and composition, equilibrium mineral modes and physical properties can be calculated by thermodynamic methods. When combined with laboratory electrical conductivity measurements and appropriate mixing laws, the bulk electrical conductivity of the Moon can be estimated. From a knowledge of the bulk conductivity the geomagnetic response at the lunar surface or in space is easily evaluated. Whereas previous studies assumed both mineralogy, and hence composition, and temperature as known a priori, the latter two parameters constitute our unknowns, determining all other parameters.

The application of this method to the Moon is facilitated because temperatures and pressures in its interior are easily reached in the laboratory, thereby allowing laboratory data to be used directly or with modest extrapolation. Also, as regards field measurements, relatively short magnetometer records ( $\sim$ days) are required for deep lunar sounding [16]. In comparison, periods up to several years are needed for sounding of the deep terrestrial mantle [23–25].

The inverse problem of estimating composition and thermal state of the Moon from electromagnetic sounding data, mass and moment of inertia it is strongly non-linear. We invoke a Markov chain Monte Carlo (MCMC) sampling algorithm to solve the inverse problem. It is formulated within a Bayesian framework, i.e. through the extensive use of probability density functions (*pdf*'s) to delineate every item of information, as laid out by [26] and [27]. The solution to the inverse problem is defined as the conjunction of these *pdf*'s and contained in the posterior *pdf* (e.g. [28–30]).

The inverse method presented here is general and provides through the unified description of phase equilibria a way of constructing planetary models where the radial variation of mineralogy and density with pressure and temperature is naturally specified, permitting a direct inversion for chemical composition and temperature. Given these parameters mineralogy, and bulk physical properties can be calculated. Inversion based on electrical conductivity is particularly intriguing, when compared to inversions based on seismic properties, because variations in conductivity with mineralogy are much stronger than the corresponding variations in elastic properties. In principle, electrical conductivity therefore offers a more sensitive means of probing planetary composition; unfortunately in practice bulk conductivity estimates are dependent on a mineralogical conductivity data base that is much more uncertain than is the case for elastic properties. For this reason, the synthesis presented here is to be viewed as a first-order model. Our purpose in constructing such a model is to establish whether such an inversion is possible. The validity of this model may be influenced by a number of factors affecting the electrical conductivity of the lunar mantle which include: poorly known effects of mineral chemistry and redox state on conductivity of mantle minerals; and how rock fabric affects conductivity.

In spite of any such reservations, we would like to point out that the goal of the present inversion, apart from trying to constrain chemical composition and selenotherm, serves a deeper purpose, namely that of integrating widely different geophysical data sets into a joint inversion. This is presently exemplified by jointly inverting electromagnetic and gravity data and is achieved by appealing to a set of parameters which are not only common to all different geophysical fields considered, but also characterises the media studied at a fundamental level.

## 2. Geophysical data and earlier lunar induction studies

Several methods have been developed to infer the electrical conductivity structure of a planet using the natural electromagnetic variations recorded on its surface. The magnetic deep sounding method, which employs only magnetic and no electric variations, is based on the assumption that an external (inducing) part induces currents in the planet creating an internal (induced) field. Using the geomagnetic variations obtained from the observations, the amplitudes and phases of the ratios of the internal to the external parts can be calculated. The ratios, formally known as transfer functions, can be used to obtain a spherically symmetric model of the planet's interior.

Measurements of the lunar inductive response to time-varying external magnetic fields when the Moon was in the solar wind or terrestrial magnetosheath have been used to infer the lunar conductivity as a function of depth. Early analyses (e.g. [9,31–33]) based on magnetometer data from Explorer 35 while in orbit (defining the incident magnetic field) and simultaneous Apollo 12 surface magnetometer data (defining incident as well as induced field) were limited to a frequency range of  $5 \cdot 10^{-4}$ – $4 \cdot 10^{-2}$  Hz. As a consequence only the upper mantle electrical conductivity structure covering the depth range 150–600 km could be inferred. Due to improved data analysis, Wiskerchen and Sonett [11] were able to obtain transfer function estimates at lower frequencies, covering the range  $10^{-3}$ – $10^{-5}$  Hz, and could therefore sound much deeper. Considering the same magnetometer data, Hood et al. [12] was able to further minimise error sources, obtaining a revised set of transfer function estimates for the same frequency range as above. The study by Hobbs et al. [34] saw one of the last attempts at inverting this data set.

Theoretical formulations of these analyses assumed, as is also the case here, perfect confinement of the induced fields by the solar wind. This model, which is known as the spherical symmetric plasma (SSP) model is not rigorously perfect, because of the incomplete confinement of the solar wind in the cavity downstream [35]. However, as discussed by Hood et al. [12] the validity of the SSP approximation increases with decreasing frequency and is justified for measurements obtained on the sunward hemisphere at sufficiently low frequency. Data analysis is reported in detail in Hood et al. [12] and the theoretical model for the interpretation of the magnetometer measurements is reviewed by Sonett [35]. Error may also stem from the assumption of incomplete external plasma confinement of induced

Table 1

Apparent resistivities,  $\rho_a$ , calculated from the estimated day-side transfer functions tabulated in [34] including error bars ( $d\rho_a$ )

Period (s)	$\rho_a$ ( $\Omega$ m)	$d\rho_a$ ( $\Omega$ m)
100,000.00	58.6	2.1
50,000.00	113.9	4.0
33,333.33	164.5	5.7
25,000.00	209.8	7.4
20,000.00	250.8	9.2
16,666.67	288.7	11.0
14,285.71	324.6	12.7
12,500.00	358.9	13.9
11,111.11	392.3	14.4
10,000.00	424.8	14.2
5000.00	693.5	36.6
3333.33	921.4	70.5
2500.00	1099.2	91.9
2000.00	1212.7	109.6
1666.67	1283.2	110.8
1428.57	1350.8	96.8
1250.00	1471.7	82.3
1111.11	1542.5	74.5
1000.00	1674.9	84.3

fields [36]. The transfer functions estimated by Hood et al. [12] and tabulated in Hobbs et al. [34] are used in the present study (see Table 1). The obtained conductivity models showed that mainly the mantle conductivity structure was constrained by the electromagnetic sounding data and that reasonable agreement between the different electromagnetic sounding studies, within order of magnitude was obtained. Results by Dyal et al. [10] were obtained using classical vacuum induction theory from an analysis of a large 6-h geomagnetic tail field transient event. The results of Hood et al. [12] were obtained by employing a Monte Carlo algorithm to randomly generate a large number of models from which were selected those that provided an adequate fit to data. Generally, the conductivity was found to rise from  $10^{-4}$ – $10^{-3}$  S/m at a few hundred km depth to roughly  $10^{-2}$ – $10^{-1}$  S/m at about 1100 km depth.

## 3. Laboratory electrical conductivity measurements and the lunar thermal profile

Turning planetary conductivity profiles into constraints on thermal state is principally done by combining the conductivity profiles with electrical conductivity measurements made on minerals as a function of temperature. Success hinges on (1) knowledge of the internal composition of the planet and hence mineralogy, and (2) laboratory measurements of the conductivity of these minerals at the appropriate temperature and

pressure regimes. In the case of the Moon, these issues are discussed further by Huebner et al. [15].

Electrical conductivity has been found to be a sum of several thermally activated processes whose temperature dependence is usually modeled by an Arrhenius equation

$$\sigma = \sigma_0 e^{-E/kT} \quad (1)$$

where  $\sigma_0$  is a constant depending upon the conduction mechanism,  $E$  is activation energy, being the sum of the energy required to produce and to move a charge carrier in the structure,  $T$  is temperature and  $k$  is Boltzmann's constant.

Temperature estimates from early electromagnetic sounding studies (limited to depths <600 km) assumed a lunar mineralogy consisting essentially of only olivine and orthopyroxene with no minor element impurities [13,14]. The resultant temperature bounds so derived were, however, found to be within 100–200 °C of the probable solidus of Ringwood and Essene [37] at shallow depths (200–400 km) and were irreconcilable with the high seismic  $Q$ -values indicated by the Apollo lunar seismic data [7] and mascon maintenance over a period of 3–4 b.y. [8]. Aware of the fact that minor constituents, e.g. alumina, can significantly effect electrical conductivity, Huebner et al. [15] and Duba et al. [38] performed additional conductivity measurements for orthopyroxenes including small amounts of alumina (these data are summarised by Hood [36] in his Fig. 6, showing that alumina significantly increases the electrical conductivity of orthopyroxene). The reason that aluminum was singled out as minor constituent is because it is assumed to be enriched in the bulk Moon compared to the chondrites and most probably also compared to the Earth. Several lines of evidence support an alumina rich lunar composition. This is based on the large crustal thickness inferred for the Moon from seismic data and its high alumina content of about (~28 wt.%) measured from highland regolith samples [39] and inferred from central-peaks of impact craters [40]. The plagioclase-rich crust is supposed to have originated by crystallisation from a molten magma sphere which might have encompassed the entire lunar globe (e.g. [41]).

To translate the experimentally derived data into bounds on temperature, Huebner et al. [15] chose a model lunar bulk composition corresponding to that proposed by Kesson and Ringwood [42], which is based on petrologic studies of mare basalts. Their model assumed an outer differentiated zone, from which the plagioclase-rich crust had been extracted, made up of approximately 76% olivine, 13% pyroxene, 10% plagioclase and 1% oxides and a primitive lunar interior

consisting of an olivine pyroxenite composition (38% olivine, 50% pyroxene, 10% plagioclase and 2% oxides). However, since conductivity measurements for arbitrary inhomogeneous mixtures of mineral phases of compositions such as these are not available, the effective conductivity of such mixtures must be determined from the data for olivine and aluminous orthopyroxenes using appropriate mixing laws. The approach considered by Huebner et al. [15] was to calculate the bulk conductivity for those minerals that exceeded 15 vol.% using a set of parallel conductors whose cross-sectional areas were each proportional to volume concentration. This formally corresponds to an averaging scheme where the individual mineral conductivities are weighted according to volume concentration. In agreement with what had been theoretically expected, the bulk conductivity model thus estimated, resulted in lower temperatures in the mantle, bringing these into accord with the other geophysical evidence.

In an attempt to further limit lunar internal temperatures, Hood et al. [16] employed a Monte Carlo scheme to first generate 18 electrical conductivity profiles that were consistent with previously derived lunar transfer function data. Electrical conductivity data were then used to convert the conductivity profiles into temperature profiles given a series of radially homogeneous olivine pyroxene mixtures that ranged from 100% olivine (Fo<sub>91</sub>) to 100% aluminous orthopyroxene containing 6.8 wt.% Al<sub>2</sub>O<sub>3</sub>. Like Sonett and Duba [13] and Duba et al. [14], they found that the composition consisting of 100% olivine yielded temperature profiles close to the Ringwood-Essene solidus at depths of 500 km, while the addition of aluminous orthopyroxene in concentrations >15–30 vol.% significantly lowered the selenotherms so that they only approached the solidus at depths >1000 km. Hood et al. [16] found that temperature limits agreed with those of Huebner et al. [15], but were generally lower by 100–200 °C at any given depth. The location of the deep moonquakes in the depth range 800–1100 km [43–45] suggests temperatures several hundred degrees below the solidus.

#### 4. Mantle mineral electrical conductivity measurements

The process of determining electrical conductivity as a function of temperature experimentally is anything but straight forward, which, early on was reflected in the scatter of measurements obtained by different laboratories. This discrepancy was mainly because of a lack of appreciation of the role played by oxygen fugacity [46].

For olivine (ol) we used the data obtained by Xu et al. [21], who found that within the temperature range from 1000 to 1400 °C the data could be fit by a single straight line, that is, with a single activation energy of  $E=1.62\pm 0.04$  eV and pre-exponential factor of  $\log(\sigma_o/\eta)=2.69\pm 0.12$  ( $\eta$  is a constant and equals 1 S/m for the remainder of the discussion), in agreement with results obtained by Constable and Duba [47]. Orthopyroxene (opx) and clinopyroxene (cpx) were investigated by Xu and Shankland [20]. For opx, containing 2.89 wt.%  $\text{Al}_2\text{O}_3$ , they determined an activation energy of  $1.8\pm 0.02$  eV and  $\log(\sigma_o/\eta)=3.72\pm 0.1$  over the temperature range 1000–1400 °C. The activation enthalpy of 1.8 eV largely resembles the value determined by Duba et al. [48] of 1.54–1.79 eV measured between 875–1375 °C, but is higher than the value of  $\sim 1.0$  eV found by Huebner et al. [15], which is most probably related to the higher alumina content of the pyroxenes, allowing for more ferric iron and therefore a higher conductivity of the pyroxene [15,38,20]. For cpx, Xu and Shankland [20] found  $E=1.87\pm 0.12$  eV and  $\log(\sigma_o/\eta)=3.25\pm 0.11$ , between 1000–1400 °C, which is somewhat higher than the activation enthalpy found earlier with values ranging from 0.97 to 1.77 eV at temperatures of 900–1300 °C [49]. The only measurements for garnet (gt) are those by Kavner et al. [19], who investigated high-pressure majoritic gt at low temperatures. However, pressures at which majoritic gt becomes stable are not achieved in the Moon. So, in the absence of measurements on appropriate gt compositions, i.e., grossular-pyrope-almandine mix-

tures, we chose to use the values determined by Kavner et al. [19], who found  $E=0.55\pm 0.1$  eV and  $\sigma_o=1\pm 0.5\cdot 10^3$  S/m over the temperature range 290–370 K. When extrapolated to mantle conditions this phase becomes highly conductive, but given that it is present at only small levels ( $< 15$  vol.%) it is of minor importance. This is supported by an inversion where we used a less conductive gt phase ( $E=1.66\pm 0.03$  eV and  $\log(\sigma_o/\eta)=3.35\pm 0.18$ , representative of the il+gt phase measured by [20]) and found only minor changes in the results. Electrical conductivities are summarised in Fig. 1A. For plagioclase we employed the results compiled by Tyburczy and Fisler [49] for synthetic anorthite over the temperature range 673–1173 K, where an activation energy of  $E=0.87$  eV and pre-exponential factor of  $\log(\sigma_o/\eta)=-0.2$  were found. In the case of spinel we face the same problem as in the case of gt as no measurements exist. However, disregarding the contribution altogether of spinel is not going to influence the results to any significant extent as spinel is present of levels of  $< 1$  vol.%.

Concerning compositional effects on conductivity, the compilations of Hood [36] and Tyburczy and Fisler [49] have suggested a dependence of the electrical conductivity of ol on Fe content and of opx on Al content. To incorporate these dependencies explicitly into our modeling we used data compiled by Hood [36] (his Fig. 6) and obtained the following first-order dependencies of  $\sigma_o$  for ol (using conductivity measurements of  $\text{Fo}_{91}$  and  $\text{Fo}_{100}$ ) and opx (using conductivity measurements for opx containing

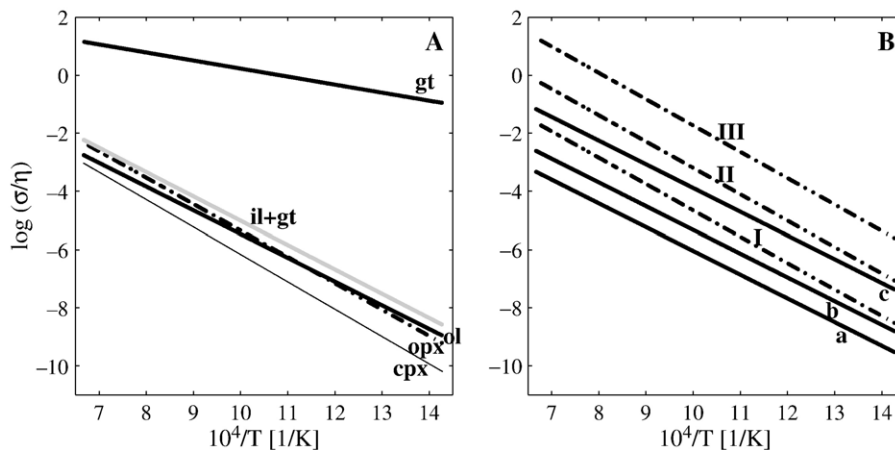


Fig. 1. Electrical conductivity as a function of temperature for the mantle minerals considered here. (A) Conductivity of major minerals versus temperature. (B) Conductivity of ol and opx as a function of temperature and composition using the relations described in the main text. Solid lines are ol conductivities at various  $x_{\text{Mg}}$ , (a) 0.95, (b) 0.9 and (c) 0.8. The dot-dashed lines are opx conductivities at various  $x_{\text{Al}}$ , (I) 0.01, (II) 0.025 and (III) 0.04. As before  $\eta=1$  S/m.

1.9 and 6.8 wt.% and  $\text{Al}_2\text{O}_3$ ), respectively, by simple interpolation at a temperature of 1000 °C

$$\log(\sigma_0^{\text{ol}}) - 14.4 \cdot (x_{\text{Mg}} - x_{\text{Mg}}^0)$$

$$\log(\sigma_0^{\text{opx}}) + 9.74 \cdot (x_{\text{Al}} - x_{\text{Al}}^0)$$

where  $x_{\text{Mg}}$  is  $n_{\text{MgO}}/[n_{\text{FeO}} + n_{\text{MgO}}]$ ,  $x_{\text{Al}}$  is tetrahedral Al content ( $n_{\text{Al}_2\text{O}_3}/[n_{\text{Al}_2\text{O}_3} + n_{\text{SiO}_2}]$ ) and  $x_{\text{Mg}}^0$  and  $x_{\text{Al}}^0$  are the compositions at which the reference value of  $\sigma_0$  is known (here 0.91 and 0.029, respectively). We did not consider the compositional dependence of cpx on either Fe or Al content as it is a minor phase. Electrical conductivities for ol and opx at various  $x_{\text{Mg}}$  and  $x_{\text{Al}}$  are summarised in Fig. 1B.

As concerns oxygen fugacity, the recent measurements of ol, opx and cpx described here were all performed using the Mo–MoO<sub>2</sub> buffer which is close to the iron–wüstite (IW) buffer [22]. The conductivity measurements from which we extracted compositional dependencies for olivine were done using a buffer of H<sub>2</sub>+CO<sub>2</sub> [50] and is also close to the IW buffer. For the conductivity dependence of opx on Al content, measurements were performed employing a CO–CO<sub>2</sub> buffer [38,15]. The oxidation state of the lunar mantle, is thought to be 0.2–1.0 log units below the IW buffer from direct measurements of intrinsic oxygen fugacities of mare basalts [51]. However, Delano [52] has pointed out that if lunar picritic glasses originated from source regions at pressures of 2 GPa in the Moon [53], the pressure dependence of the C–CO–CO<sub>2</sub> buffer would cause the redox state at those pressures in the Moon to be ~1.5 log units  $f\text{O}_2$ , above the IW buffer. Given this discrepancy we shall presently disregard effects of oxygen fugacity. Furthermore, we will also neglect the contributions which might arise from the presence of grain boundaries, porosity, melt and water as these are thought to represent only a small fraction of the bulk conductivity. Effects of porosity can easily be disregarded as these are annealed due pressure and are only important if the uppermost crust is considered, which is not the case here. Water is present at levels less than ppb [39] and will thus not give rise to any large contribution to conductivity. Melt might potentially be important, although only for the lowermost mantle where a partially molten state has been tentatively inferred to exist [54]. However, as the electromagnetic sounding data considered here are not sensitive to such depths, melt contribution to electrical conductivity can effectively be disregarded. As contributions from grain boundaries are believed to give rise to only a minor fraction of bulk terrestrial conductivity [22], we will not consider these in the case of the Moon either. While we

model the temperature variation of electrical conductivity, we neglect effects of pressure. There is evidence that this effect is of minor importance. First of all, because pressure increases in the Moon are very small (the pressure at the center of the Moon is ~4.7 GPa which is reached at a depth of ~150 km in the Earth). Second, in a recent study by Xu and Shankland [21] where pressure effects on the electrical conductivity of mantle olivine were investigated, mainly positive activation volumes were found, which led the authors to suggest that for the terrestrial upper mantle (80–200 km depth) neglecting pressure effects on olivine conductivity were justified.

## 5. Solving the inverse problem—theoretical preliminaries

The sequence of steps that are usually employed in solving an inverse problem could be captured as follows. Parametrisation of the physical system under study, by which is meant enumerating a set of model parameters that completely characterise the system, i.e. we define a set of coordinates  $\mathbf{m} = \{\mathbf{m}_1, \mathbf{m}_2, \dots\}$  in the model space  $\mathcal{M}$ . Next follows forward modeling, that is, the act of using  $\mathbf{m}$  to predict a set of measured parameters  $\mathbf{d} = \{\mathbf{d}_1, \mathbf{d}_2, \dots\}$  defined in some data space  $\mathcal{D}$ , through the application of physical laws pertinent to the problem at hand. The final step involves inverse modeling which means making inferences about physical systems ( $\mathbf{m}$ ) from real data ( $\mathbf{d}_{\text{obs}}$ ). In presenting the solution to the inverse problem, we shall follow in the steps of 26 and 27.

Central to the conjecture is the notion of a *state of information* over a parameter set, which is described using a *probability density function* (*pdf*) over the corresponding parameter space. This includes the information contained in measurements of the observable parameters  $\rho_{\mathcal{D}}(\mathbf{d})$ , the a priori information on model parameters  $\rho_{\mathcal{M}}(\mathbf{m})$ , combined into a joint *pdf*  $\rho(\mathbf{d}, \mathbf{m})$  and the information on the physical correlations between observable and model parameters, also written as a joint *pdf*,  $\Theta(\mathbf{d}, \mathbf{m})$ . Solving the inverse problem, then, shall be formulated as a conjunction of these *pdf*'s, representing all the information we possess about the system and from which we can extract, by suitable methods, answers to selected queries. The extensive use of *pdf*'s has the advantage in that the solution to the inverse problem is presented in the most generic way, thereby implicitly incorporating any non-linearities [26]. The solution to the inverse problem is given by

$$\sigma(\mathbf{d}, \mathbf{m}) = k \frac{\rho(\mathbf{d}, \mathbf{m})\Theta(\mathbf{d}, \mathbf{m})}{\mu(\mathbf{d}, \mathbf{m})} \quad (2)$$

where  $\sigma(\mathbf{d}, \mathbf{m})$  and  $\mu(\mathbf{d}, \mathbf{m})$  represent the *a posteriori* and homogeneous states of information, respectively. This form of the solution to the general inverse problem is essentially seen to be defined as a combination of experimental, a priori and theoretical information. Introducing the functions (1)  $\Theta(\mathbf{d}, \mathbf{m}) = \theta(\mathbf{d}|\mathbf{m})\mu_{\mathcal{M}}(\mathbf{m})$ , which states that our physical theory can be written in the form of a *pdf* for  $\mathbf{d}$  given any possible  $\mathbf{m}$ , where  $\mu_{\mathcal{M}}(\mathbf{m})$  is the homogeneous *pdf* over the model space, (2)  $\rho(\mathbf{d}, \mathbf{m}) = \rho_{\mathcal{D}}(\mathbf{d})\rho_{\mathcal{M}}(\mathbf{m})$ , i.e. that prior information on observable parameters has been gathered independently of the prior information on model parameters and (3)  $\mu(\mathbf{d}, \mathbf{m}) = \mu_{\mathcal{D}}(\mathbf{d})\mu_{\mathcal{M}}(\mathbf{m})$ , that in the homogeneous limit of  $\rho_{\mathcal{M}}(\mathbf{m})$ , the posterior *pdf* in the model space  $\mathcal{M}$  can be written as

$$\sigma_{\mathcal{M}}(\mathbf{m}) = k\rho_{\mathcal{M}}(\mathbf{m}) \int_{\mathcal{D}} \frac{\rho_{\mathcal{D}}(\mathbf{d})\theta(\mathbf{d}|\mathbf{m})}{\mu_{\mathcal{D}}(\mathbf{d})} d\mathbf{d} \quad (3)$$

which is generally summarised as

$$\sigma_{\mathcal{M}}(\mathbf{m}) = k\rho_{\mathcal{M}}(\mathbf{m})\mathcal{L}(\mathbf{m}) \quad (4)$$

where  $k$  is a constant and  $\mathcal{L}(\mathbf{m})$  the likelihood function, measuring how well a given model fits the observed data.

Eq. (2), or equivalently Eq. (4), is defined as the solution to the general inverse problem [26,27]. Having obtained  $\sigma_{\mathcal{M}}(\mathbf{m})$ , we can proceed to evaluate any estimator (mean, median, maximum likelihood, uncertainty, etc.) for any given model parameter that we might be interested in or simply consider a sequence or samples from  $\sigma_{\mathcal{M}}(\mathbf{m})$ .

Let us now turn to the problem of actually obtaining  $\sigma_{\mathcal{M}}(\mathbf{m})$ . The basic idea is to design a random walk in the model space, that, if unmodified, samples some initial probability distribution. By subsequently applying certain probabilistic rules, we can modify the random walk in such a way that it will sample some target distribution. The Metropolis-Hastings algorithm [55,56], which is a MCMC method, can be shown to be the one that most efficiently achieves this goal. The MCMC method is so named, because it is random (Monte Carlo) and has got shortest possible memory, that is, each step is only dependent upon the previous step (Markov chain).

To sample the posterior *pdf*  $\sigma_{\mathcal{M}}(\mathbf{m}) = k\rho_{\mathcal{M}}(\mathbf{m})\mathcal{L}(\mathbf{m})$  using the Metropolis algorithm we shall invoke the following sequence of steps, assuming that we are able to sample the prior *pdf*. Let us start out from some point  $\mathbf{m}_i$  in the model space. We now wish to make a transition to another point  $\mathbf{m}_j$ . The acceptance of the proposed transition is governed by the following rule

- if  $\mathcal{L}(\mathbf{m}_j) \geq \mathcal{L}(\mathbf{m}_i)$ , then accept the proposed transition to  $\mathbf{m}_j$ ;

- if  $\mathcal{L}(\mathbf{m}_j) < \mathcal{L}(\mathbf{m}_i)$ , then decide randomly to move to  $\mathbf{m}_j$  or to remain at  $\mathbf{m}_i$ , with transition probability  $P_{i \rightarrow j}$  of accepting the move to  $\mathbf{m}_j$ ;

$$P_{i \rightarrow j} = \frac{\mathcal{L}(\mathbf{m}_j)}{\mathcal{L}(\mathbf{m}_i)}$$

- if the transition  $i \rightarrow j$  is accepted, then  $\mathbf{m}_{i+1} = \mathbf{m}_j$  else  $\mathbf{m}_{i+1} = \mathbf{m}_i$  and repeat the above steps.

This iterative scheme will, if given steps enough, sample the posterior distribution.

It is obvious from the preceding developments that the solution to the general inverse problem, as presented here, being a *pdf*, cannot be described by one single realisation like the mean or the median model or even the maximum likelihood model, but is best characterised by looking at samples from the posterior *pdf*. This approach adheres to what is advocated by Tarantola [27,p,47], who states: “The common practice of plotting the ‘best image’ or the ‘mean image’ should be abandoned, even if it is accompanied by some analysis of error and resolution”. Of course some situations might nonetheless call for the calculation of certain moments (mean, covariances, etc.) which, if needed, are easily evaluated using the sampled models. As concerns the question of analysis of the posterior *pdf*, Tarantola [27] strongly advocates the use of, what Mosegaard and Tarantola [28] termed the movie strategy for inverse problems as the most natural way of displaying the information contained in a *pdf*. This involves displaying a set of images, i.e. models, from the *pdf*. A large number of randomly generated models from the posterior *pdf* will give us a good understanding of the general information contained in it. Also, by displaying in the same manner samples from the prior *pdf*, not only allows us to verify that prior information is being adequately sampled and moreover, by comparing prior and posterior images we gain valuable insight into how much information is actually provided by data. Finally, we can also analyse  $\sigma_{\mathcal{M}}(\mathbf{m})$  by simply asking questions of a very general form

$$P(\mathbf{m} \in \mathcal{E}) = \int_{\mathcal{E}} \sigma_{\mathcal{M}}(\mathbf{m}) d\mathbf{m} \quad (5)$$

i.e. what is the probability that a model  $\mathbf{m}$  belongs to a given region  $\mathcal{E} \in \mathcal{M}$  of the model space?

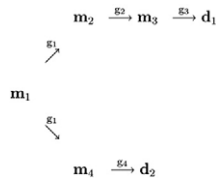
## 6. Constructing the forward model

To solve a forward problem means to predict error-free values of observable parameters, signified by  $\mathbf{d}$  and termed predicted or calculated data, that corresponds to

a given model  $\mathbf{m}$ . This statement is usually condensed into the expression

$$\mathbf{d} = g(\mathbf{m}) \quad (6)$$

where  $g$  is a (usually non-linear) functional relation governing the physical laws that relate model and data, expressing our mathematical model of the physical system under study. Let us break Eq. (6) up into a number of forward modeling sequences



where  $\mathbf{m}_1$  is an assumed starting composition and selenotherm,  $g_1$  is the forward operator embodying the Gibbs free energy minimisation routine, calculating mineral phase proportions (modal mineralogy) and their physical properties, in the form of density, contained in the model parameter vectors  $\mathbf{m}_2$  and  $\mathbf{m}_4$ , respectively.  $g_2$  embodies the combination of modal mineralogies with laboratory electrical conductivity measurements and an appropriate mixing law,  $\mathbf{m}_3$  contains the bulk conductivity model,  $g_3$  is the physical law connecting the electrical conductivity profile to the electromagnetic transfer functions ( $\mathbf{d}_1$ ), and finally,  $g_4$  is the operator that calculates mass and moment of inertia, contained in the data vector  $\mathbf{d}_2$ . Before taking a closer look at each single forward operator, let us briefly delineate our physical model of the Moon.

We assume a spherically symmetric model of the Moon, which is divided into three concentric shells whose thicknesses are variable. The three layers correspond to crust, mantle and core. The outermost shells are described by the model parameters: thickness  $d$ , composition  $c$  and temperature  $T$ . The physical properties of the core are specified by the model parameters: size, density and electrical conductivity. The simplification for the core layer was made because we lack the thermodynamic data required to model metallic compositions. The temperature  $T$  is defined at six fixed radial nodes. To determine the mineralogical structure and corresponding mass density it is also necessary to specify the pressure profile in addition to composition and temperature.

### 6.1. Solving the forward Problem I—petrologic modeling

Crust and mantle compositions were allowed to vary within the system CaO–FeO–MgO–Al<sub>2</sub>O<sub>3</sub>–SiO<sub>2</sub> (here-

after abbreviated CFMAS). This system was chosen in order to model the greatest fraction of the likely lunar compositions while minimising the number of variables in the inversion. The CFMAS system describes more than 98% of the lunar bulk composition estimates given by [57] and the model results presented in the following sections show that the geophysical observations can be matched using this simple system. Furthermore the thermodynamic properties of the CFMAS system are relatively well known when compared with systems including additional components, such as NaO<sub>2</sub> and TiO<sub>2</sub> [57]. Minor components such as Na<sub>2</sub>O (e.g. [58]) and redox state [22] can significantly influence the electrical conductivity of minerals, but these effects are not known or too poorly quantified to be incorporated here. Other components that are also not considered here include Cr<sub>2</sub>O<sub>3</sub>, NiO, MnO and TiO<sub>2</sub>, because of lack of experimental data on the effect of their physical properties and phase equilibria. The lunar mineralogy is assumed to be dictated by equilibrium and is computed together with mineral densities from thermodynamic data for a given model pressure, temperature and bulk composition by Gibbs free energy minimization [59]. These calculations were made taking into consideration the non-stoichiometric phases summarized in Table 2 and the stoichiometric phases and species in the thermodynamic data compilation of [60]. The equilibrium assumption is dubious at low temperature (e.g. [61]). In recognition of this limitation, if a model required a temperature below 1073 K, then the equilibrium mineralogy was calculated at 1073 K. Thermodynamic properties were then computed for the assemblage so obtained at the temperature of interest at 31 fixed radial points (this number was found to provide more than adequate resolution for the present purposes) starting from the surface and continuing down to the CMB. The thickness of the individual layers was chosen in such a way that the highest resolution, i.e. thin layers, were

Table 2  
Solution notation, formulae and model sources

Symbol	Solution	Formula	Source
crd	cordierite	[Mg <sub>x</sub> Fe <sub>1-x</sub> ] <sub>2</sub> Al <sub>4</sub> Si <sub>5</sub> O <sub>18</sub>	ideal
cpx	clinopyroxene	CaMg <sub>x</sub> Fe <sub>1-x</sub> Si <sub>2</sub> O <sub>6</sub>	[60]
gt	garnet	[Fe <sub>x</sub> Ca <sub>y</sub> Mg <sub>1-x-y</sub> ] <sub>3</sub> Al <sub>2</sub> Si <sub>3</sub> O <sub>12</sub> , $x+y \leq 1$	[60]
ol	olivine	[Mg <sub>x</sub> Fe <sub>1-x</sub> ] <sub>2</sub> SiO <sub>4</sub>	[60]
opx	orthopyroxene	[Mg <sub>x</sub> Fe <sub>1-x</sub> ] <sub>2-y</sub> Al <sub>2y</sub> Si <sub>2-y</sub> O <sub>6</sub>	[60]
sp	spinel	Mg <sub>x</sub> Fe <sub>1-x</sub> Al <sub>2</sub> O <sub>3</sub>	ideal

Unless otherwise noted, the compositional variables  $x$  and  $y$  may vary between zero and unity and are determined as a function of the computational variables by free-energy minimization.

placed in the crust, with layer thickness increasing at the expense of resolution as we go down through the mantle.

### 6.2. Solving the forward Problem II—calculating bulk rock electrical conductivity

As rocks are a natural mixture of minerals and are inhomogeneous due to their mixed mineral content, the effective conductivity of an aggregate is sensitive to its microstructure. However, in the absence of information on texture, one can consider conduction models in terms of macroscopic mixture theory which is usually organised into three general categories, including exact results, bounds and estimates [62]. Xu et al. [22] discuss the various mixture theories as applied to the estimation of bulk electrical conductivity from individual minerals. Given that Xu et al. [22] have shown that the variations between different calculated conductivities are of the order of 0.1 log unit or less, we employ the geometric mean [18], computed as

$$\sigma(r) = \sigma_{GM}(r) = \prod_i \sigma_i^{x_i(r)}(r)$$

where  $\sigma_i(r)$  is the conductivity of phase  $i$  and  $x_i(r)$  its volume fraction as a function of radius  $r$ .

### 6.3. Solving the forward Problem III—estimating transfer functions for a spherically symmetric conductivity model

Estimating the internal conductivity structure of a sphere from transfer functions is a well-expounded problem (e.g. [63,64]). Because the Moon lacks an insulating atmosphere, the boundary conditions in the case of lunar induction are different to those applied to the Earth. However, most of the approaches that have been derived for the terrestrial case can nonetheless be applied to the Moon if different definitions of the transfer functions are used [64].

The transfer function traditionally employed in studying lunar induction,  $\Gamma$ , is defined as  $(B_e + B_i)/B_e$ , i.e. the absolute value of the ratio of total (external + induced) to external magnetic fields. This transfer function is related to the  $C$ -response often used in terrestrial induction studies by means of [34, Eq. (11)]

$$|C(\omega)| = a/2\Gamma(\omega) \quad (7)$$

where  $a$  is lunar radius. In deriving this relationship we assumed, as done previously [12,32–35], perfect confinement of the induced fields by the solar wind (SSP theory) and the presence of a uniform external (inducing) field.

Given a 1D conductivity structure  $\sigma(r)$ , that is, a conductivity model which only depends on radius, we solve the induction equation numerically for the function  $G(r, \omega)$

$$\frac{d^2 G}{dr^2} - \left[ i\omega\mu_0\sigma(r) + \frac{2}{r^2} \right] G = 0 \quad (8)$$

where  $\mu_0$  is vacuum permeability, with the boundary condition  $G(a, \omega) = 1$  for all frequencies  $\omega$ . Once  $G(r, \omega)$  is known for a given conductivity distribution and at various frequencies  $\omega$ , the lunar transfer function is determined from

$$\Gamma(\omega) = \left| \frac{B_e(\omega) + B_i(\omega)}{B_e(\omega)} \right| = \left| \frac{a}{2} \frac{dG(r, \omega)}{dr} \right|_{r=a} \quad (9)$$

[34, Eqs. (3) and (4)]. Rather than using the transfer function  $\Gamma$  we employ apparent resistivities which are related to the admittance or  $C$ -response through the following relation

$$\rho_a(\omega) = \omega\mu_0 |C(\omega)|^2 \quad (10)$$

Combining Eqs. (7) and (10), then, provides the desired relationship between apparent resistivity and transfer function for the lunar case

$$\rho_a(\omega) = \frac{\omega\mu_0 a^2}{4\Gamma^2(\omega)} \quad (11)$$

which can be compared to observed apparent resistivities.

### 6.4. Solving the forward Problem IV—estimating mass and moment of inertia

Once the mineral densities as a function of depth have been calculated we can estimate lunar mass and moment of inertia using the simple relations

$$I = \frac{8\pi}{3} \int \rho(r)r^4 dr, \quad M = 4\pi \int \rho(r)r^2 dr. \quad (12)$$

The adopted values are  $M = 7.3477 \pm 0.0033 \cdot 10^{22}$  kg and  $I/MR^2 = 0.3935 \pm 0.0002$  [65], based on the moment of inertia value of 0.3931 obtained through the analysis of Lunar Prospector [66] and resealed to a mean radius  $R$  of 1737.1 km.

## 7. Solving the inverse problem

### 7.1. Parameterization of the Problem

#### 7.1.1. Composition, temperature and layer thickness

Our spherically symmetric model of the Moon is divided into 3 layers, a crust, a mantle and a core.

Thermodynamic modeling is restricted to the layers comprising crust and mantle, as metallic Fe is not included in the compositional space. Crust and mantle layers are variable in size, modeled by depth  $d$  and are assumed to be uniformly distributed within the following intervals  $30 < d_{\text{crust}} < 60$  km,  $d_{\text{crust}} < d_{\text{mantle}} < d_{\text{CMB}}$ , where  $d_{\text{CMB}}$  is the depth to the core mantle boundary and the radius of the Moon is anchored at  $r_{\text{moon}} = 1737$  km. The depth to the CMB is determined as  $d_{\text{CMB}} = r_{\text{moon}} - r_{\text{core}}$ , where  $r_{\text{core}}$  is the variable core radius. The core is parametrised in terms of its radius, density ( $\rho_{\text{core}}$ ) and bulk electrical conductivity ( $\sigma_{\text{core}}$ ). These are distributed uniformly in the intervals  $0 < r_{\text{core}} < 400$  km,  $\rho_{\text{m}} < \rho_{\text{core}} < \rho_{\text{c}}$ , where  $\rho_{\text{m}}$  is the value of  $\rho$  at the base of the mantle and  $\rho_{\text{c}} = 7.5$  g/cm<sup>3</sup> (density of pure  $\gamma$ -Fe at the conditions at the center of the Moon [57]).  $\sigma_{\text{core}} \in [\sigma_{\text{m}}; \sigma_{\text{c}}]$ , where  $\sigma_{\text{m}}$  is likewise the electrical conductivity at the base of the mantle and  $\sigma_{\text{c}}$  is some upper bound, here  $10^5$  S/m.

Temperature  $T$  is parametrised at 6 fixed nodal points, corresponding to depths of 0, 200, 400, 500, 1000 and 1700 km. At each of these nodes the logarithm of  $T$  is uniformly distributed in the interval  $T_k \in [T_{k-1}; T_{k+1}]$ , with the added constraint,  $\dots T_{k-1} \leq T_k \leq T_{k+1} \dots$ , to prevent temperature models from decreasing as a function of depth. We have chosen the peridotite solidus of [67] as an

upper bound (the peridotite solidus is only used as a rough guide to the melting behaviour of silicates), here labeled  $T_{\text{p}}$ , so that in any given layer  $k$  there also exists the constraint  $T_k < T_{\text{p}}^k$ . Surface temperature is held constant at 0 °C.

Crust and mantle are additionally parametrised using the composition  $c$ , which designates the wt.% of the elements CaO–FeO–MgO–Al<sub>2</sub>O<sub>3</sub>–SiO<sub>2</sub>. These are log-uniformly distributed within certain intervals, corresponding to  $1 < \text{CaO} < 8$  wt.%,  $5 < \text{FeO} < 15$  wt.%,  $20 < \text{MgO} < 55$  wt.%,  $1 < \text{Al}_2\text{O}_3 < 8$  wt.% and  $35 < \text{SiO}_2 < 55$  wt.% and with the added constraint that in each of the two layers  $\sum_i c_i = 100$  wt.%. Moreover, the minor elements ratio  $\text{Ca}/\text{Al} \in [0.5; 2]$ . For the crust we assumed the composition of [39] (CaO=16 wt.%, FeO=6.5 wt.%, MgO=7 wt.%, Al<sub>2</sub>O<sub>3</sub>=25 wt.% and SiO<sub>2</sub>=45.5 wt.%) and varied the concentration of the five elements by 5 wt.% around this model of the crust.

### 7.1.2. Activation energy and pre-exponential factor

As already pointed, given the importance of mineral electrical conductivities in determining internal temperatures, we modeled  $E$  and  $\sigma_{\text{o}}$ , by assuming that these are distributed according to the values described earlier (see Section 4).

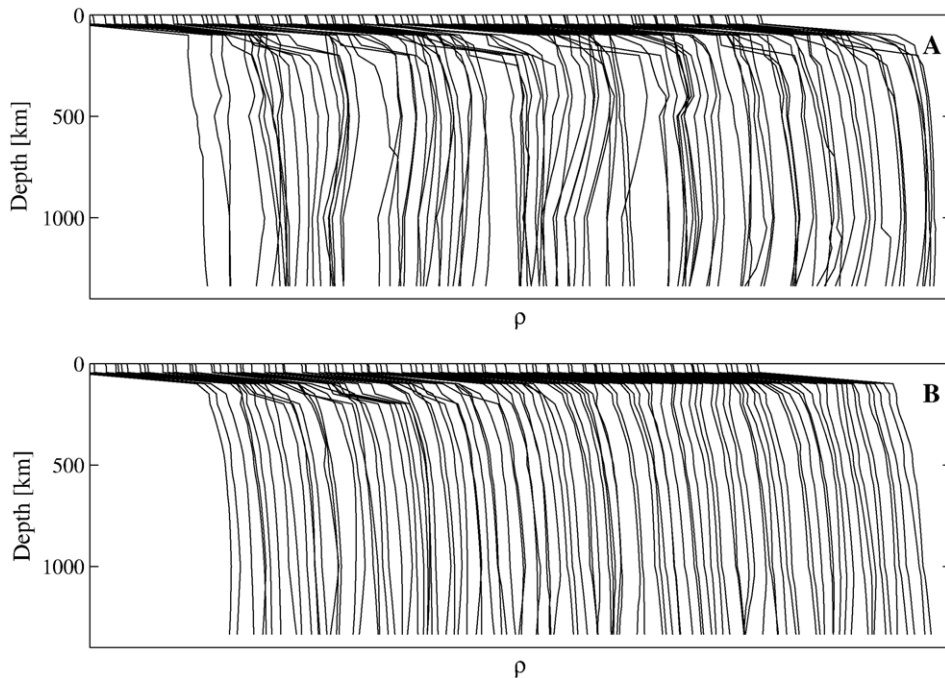


Fig. 2. Collection of 100 models taken randomly from the prior (A) and posterior (B) *pdf*'s showing density as a function of depth. Separation between individual models is 10 g/cm<sup>3</sup>. Comparison of prior and posterior models provides a valuable insight into the information contained in the data. Prior models seem 'messy', reflecting the few prior constraints imposed on these parameters, whereas posterior models seem 'well behaved'.

For the major mineral phases ol, opx, cpx, gt and plg, we assumed the values of  $E$  and  $\sigma_o$  described in Section 4 and varied these uniformly by amounts  $\pm\Delta E$  and  $\pm\Delta\sigma_o$ , corresponding to the uncertainty estimates also quoted in Section 4. In other words prior information on these parameters is described by a uniform distribution in the interval  $[E-\Delta E; E+\Delta E]$  and  $[\sigma_o-\Delta\sigma_o; \sigma_o+\Delta\sigma_o]$ .

7.1.3. Mineralogy, density and bulk electrical conductivity

From a knowledge of composition, temperature and pressure we can use free energy minimisation to obtain the mineral phases that are stable at these conditions as well as its physical properties, in the form of the density and electrical conductivity. These parameters were evaluated at 31 fixed radial nodes from the surface down to the CMB using the following parametrization. Layers 1 and 2 are 5 km thick, layers 3–7 are 10 km thick, while the remaining layers thicknesses are 50 km. In sampling density profiles, we introduced a penalty function to ensure that the

algorithm is less likely to accept density models that decrease as a function of depth.

7.2. Prior sampling of models

This, then, describes prior information,  $\rho_{\mathcal{M}}(\mathbf{m})$ , on model parameters and our model parameter vector is thus given by  $\mathbf{m} = \{c_{ij}, T_k, d_j, r_{\text{core}}, \rho_{\text{core}}, \sigma_{\text{core}}, E_l, \sigma_o^l\}$  consisting of 29 parameters in all. To best summarise prior information we have displayed in Fig. 2A a collection of 100 density models taken randomly from the prior *pdf*.

7.3. Posterior sampling of models

Having considered prior sampling of models we can now turn our attention to sampling the posterior *pdf*, which, according to Eq. (4), is obtained by considering data through the likelihood function  $\mathcal{L}(\mathbf{m})$ . We assume that the observational uncertainties and calculation errors are independent among the different geophysical methods employed and additionally make the assumption

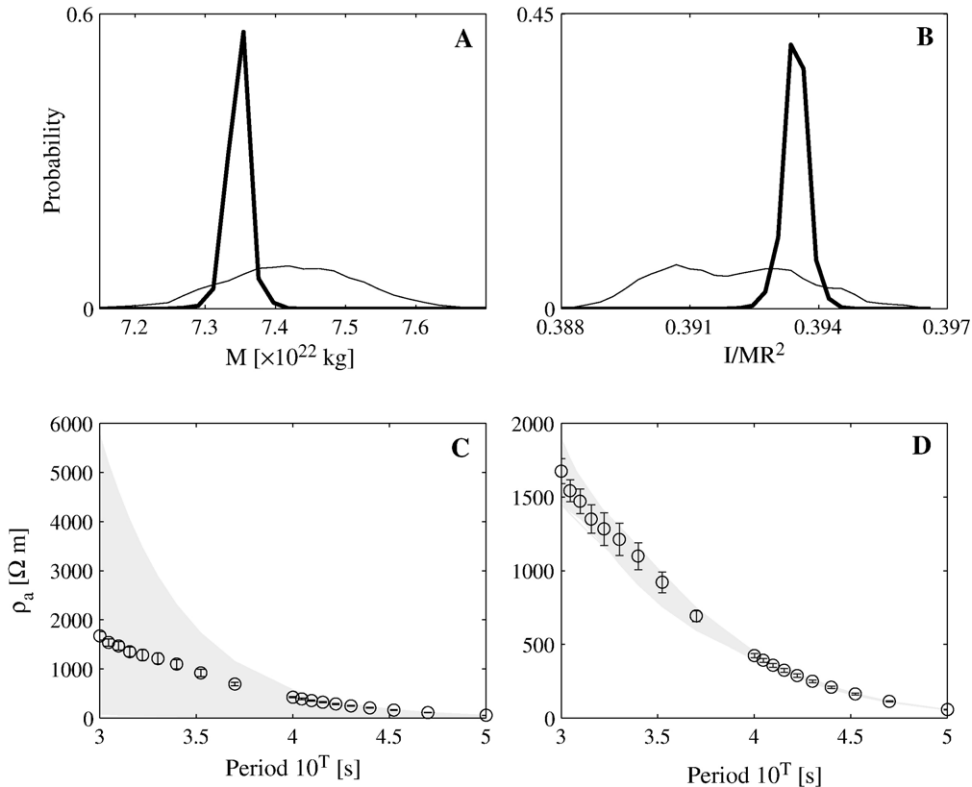


Fig. 3. Prior and posterior data fit. By comparing prior and posterior we can gauge how much information is contained in the data. The extreme narrowing of the posterior data distribution clearly indicates this in ease of both (A) mass and (B) moment of inertia (thin lines indicate prior *pdf*'s and heavy lines posterior *pdf*'s). Sampled prior (C) and posterior (D) transfer functions with observations superimposed, including error bars (observed transfer functions and associated uncertainties are summarised in Table 1).

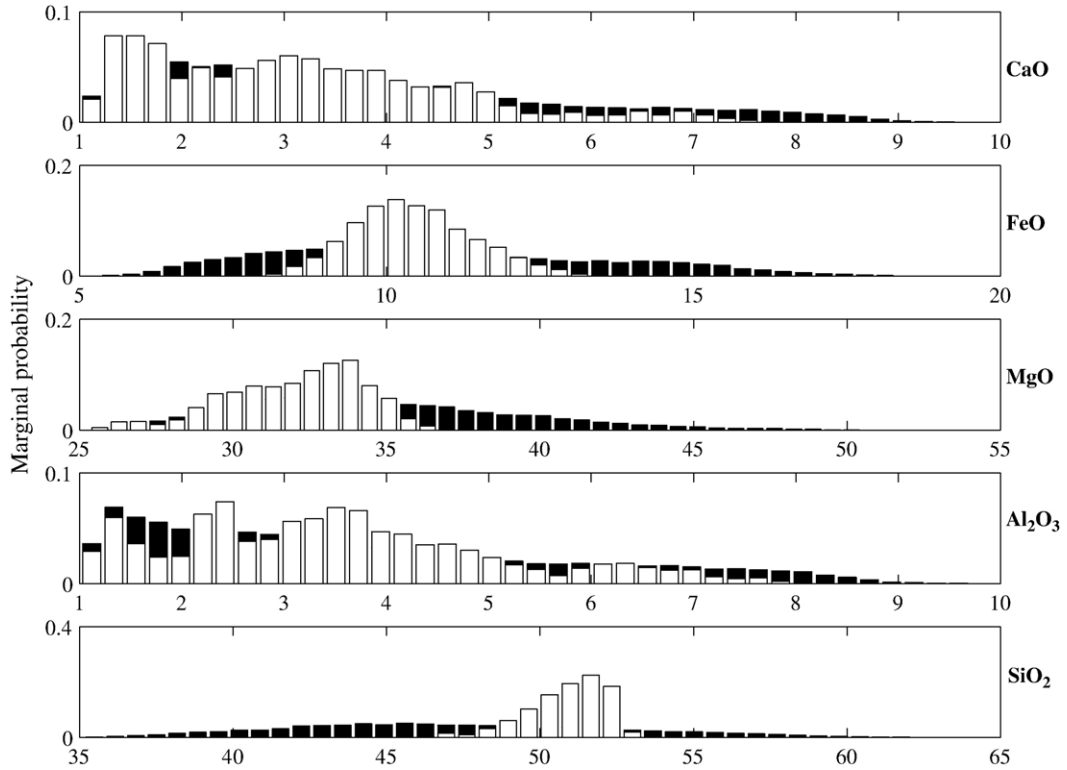


Fig. 4. Prior (black) and posterior (white) marginal *pdf*'s for the oxide elements in the CFMAS system (marked to the right of each panel) making up the mantle composition. Note that as we are not plotting the logarithm of the individual parameters, we do not obtain homogeneous distributions, but ones that are skewed.

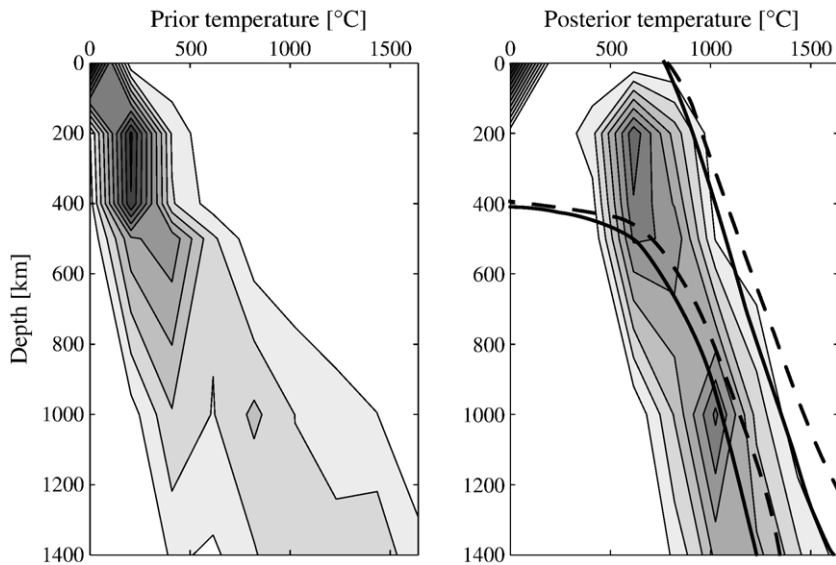


Fig. 5. Marginal prior (left panel) and posterior (right panel) *pdf*'s depicting sampled temperature models as a function of depth from the surface to the core mantle boundary (CMB). At the 6 fixed depth nodes a histogram reflecting the marginal probability distribution of sampled temperatures has been set up. By lining up these marginals, temperature as a function of depth can be envisioned as contours directly relating its probability of occurrence. Shades of gray between white and black indicating, respectively, least and most probable outcomes. Solid lines indicate the temperature bounds obtained by Hood et al. [12] using pyroxenes containing 6.8 wt.%  $\text{Al}_2\text{O}_3$  and dashed lines are for pyroxenes with 1.9 wt.%  $\text{Al}_2\text{O}_3$ .

that data uncertainties can be modeled using a Gaussian distribution. With this in mind, the likelihood function takes the following form

$$\mathcal{L}(\mathbf{m}) \propto \exp \left\{ \sum_i \frac{[d_{\text{obs},i}^{p_a} - d_{\text{cal},i}^{p_a}(\mathbf{m})]^2}{2s_i^2} - \frac{[d_{\text{obs}}^M - d_{\text{cal}}^M(\mathbf{m})]^2}{2s_M^2} - \frac{[d_{\text{obs}}^l - d_{\text{cal}}^l(\mathbf{m})]^2}{2s_l^2} \right\} \quad (13)$$

where  $d_{\text{obs}}$  denotes observed data,  $d_{\text{cal}}(\mathbf{m})$  is synthetic data computed using model  $\mathbf{m}$  with superscripts alluding to the particular geophysical observation and  $s$  is the uncertainty on either of these.

We are now in the position to actually run the Metropolis-Hastings algorithm. Let us assume that we are currently residing at point  $\mathbf{m}_i$  in the model space. From here we wish to make a transition to the neighbouring point  $\mathbf{m}_j$ . This is done in the following manner. In a given iteration we start off by choosing a shell at random, that is, either the crust, mantle or core, and then randomly change the parameters describing

this shell, using the proposal (prior) distribution just discussed. The adopted proposal distribution has a burn-in time of about 1000 iterations. Once this point has been reached we retain samples for analysis. In all we sampled 1 million models from which we retained  $10^4$ . The overall acceptance rate was about 40%.

There are a number of technical issues, concerning the Metropolis-Hastings algorithm which have not been mentioned. These include the question of when convergence has been reached, how many samples are needed and the problem of acquiring independent samples. To ensure convergence of the MCMC algorithm we monitored the time series of all output parameters from the algorithm. We also chose different initial conditions in the model space (different starting compositions) and compared the results from these different runs to verify that the algorithm converged to similar likelihood values. Concerning the number of samples that are needed to provide a good representation of the posterior *pdf*, we adopted the criterion that once there are no longer any significant changes to the

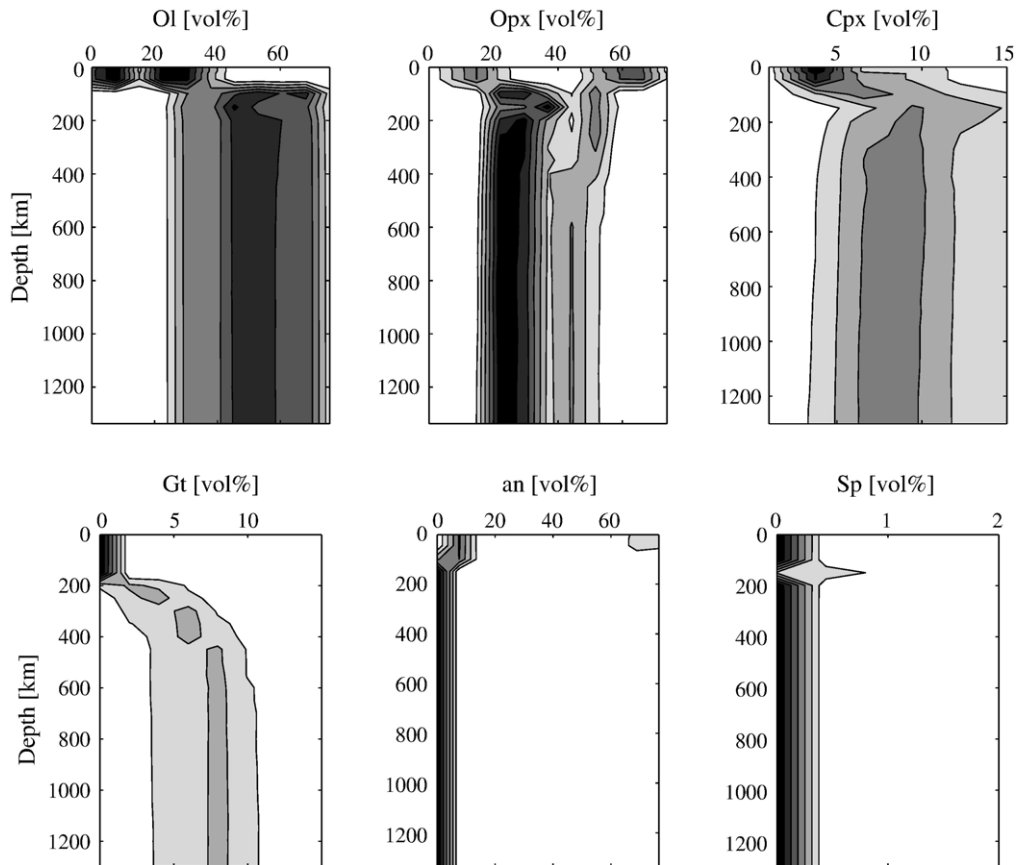


Fig. 6. Marginal posterior *pdf*'s of major minerals, showing the vol.% of each phase as a function of depth from the surface to the CMB. The marginals have been constructed in the same manner as in Fig. 5. Shades of gray as in Fig. 5.

characteristics of the posterior *pdf* we have sampled an adequate number. To ensure near-independent samples, we introduced an ‘elapse time’ between retention of samples. By analysing the autocorrelation function of the fluctuations of the likelihood function we found an elapse time of 100.

Fig. 2B shows a collection of 100 density models taken randomly from the posterior *pdf*. A direct comparison with the prior models (Fig. 2A) provides us with an indication of those structures in the Moon that are well resolved and those that are ill resolved. Well-resolved structures are those that tend to appear frequently, whereas ill-resolved structures tend to appear infrequently.

## 8. Results

Our model of the Moon assumes spherical symmetry, obviating the consideration of heterogeneity. Although the Moon is thought to be heterogeneous, especially as concerns crustal structure [68], this will not seriously affect our results as the contribution of the crust to the electromagnetic induction signal is almost negligible given the low temperatures in this part of the Moon. Moreover, as remarked by Herbert et al. [69], to further constrain the shallow structure (depths < 450 km), additional measurements at higher frequency are needed.

### 8.1. Predicted data

Fig. 3 shows prior and posterior distributions of calculated data from which we can see that excellent data fits are obtained.

### 8.2. Composition and thermal state

Fig. 4 displays composition  $c$  for the mantle in the form of 1D prior and posterior marginals, showing that  $c$  is being constrained by data (we are presently only concerned with the mantle as crustal structure is not well constrained by the data). Temperature models are shown in Fig. 5 using 1D marginal prior and posterior *pdf*'s. Like  $c$ , the posterior marginals for  $T$  are also seen to be significantly narrowed, signaling that inversion of the data considered here are able to provide information on composition and thermal state.

From Fig. 5 we can see that while our thermal profiles are broadly in agreement with previous work [12,15,17], most probable temperatures in the lower mantle are slightly lower than earlier results. This is probably due to the higher activation energy of opx as determined recently [20] in comparison to previous investigations [15,48], which, as discussed in Section 4, is related to the higher alumina content and results in a higher conductivity of the pyroxenes. The inferred temperatures are well below the probable solidus

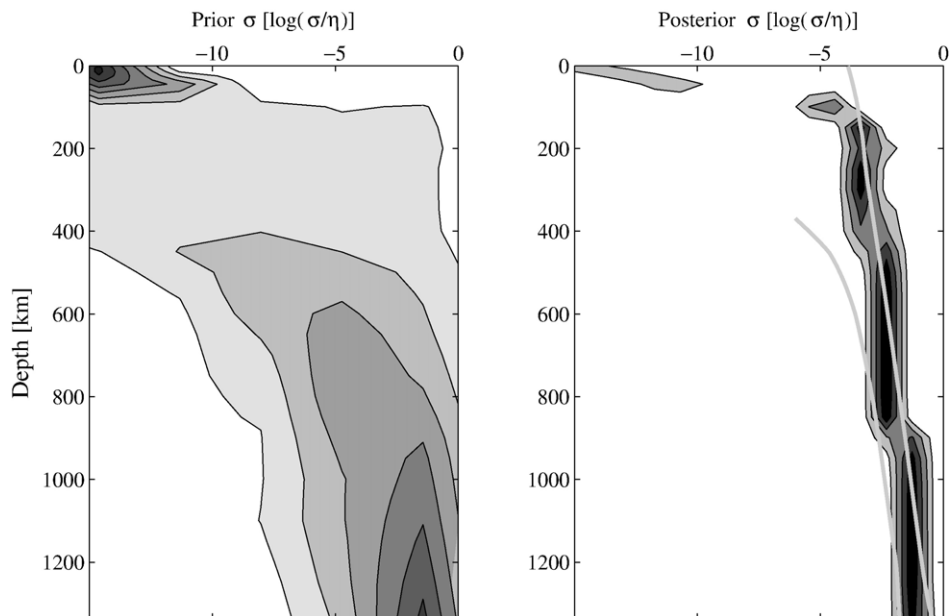


Fig. 7. Marginal prior (left panel) and posterior (right panel) *pdf*'s depicting sampled bulk conductivity profiles as a function of depth from the surface to the CMB. Log signifies base 10 logarithm. Shades of gray as before. Solid gray lines indicate the bounds on conductivity derived by Hood et al. [12].

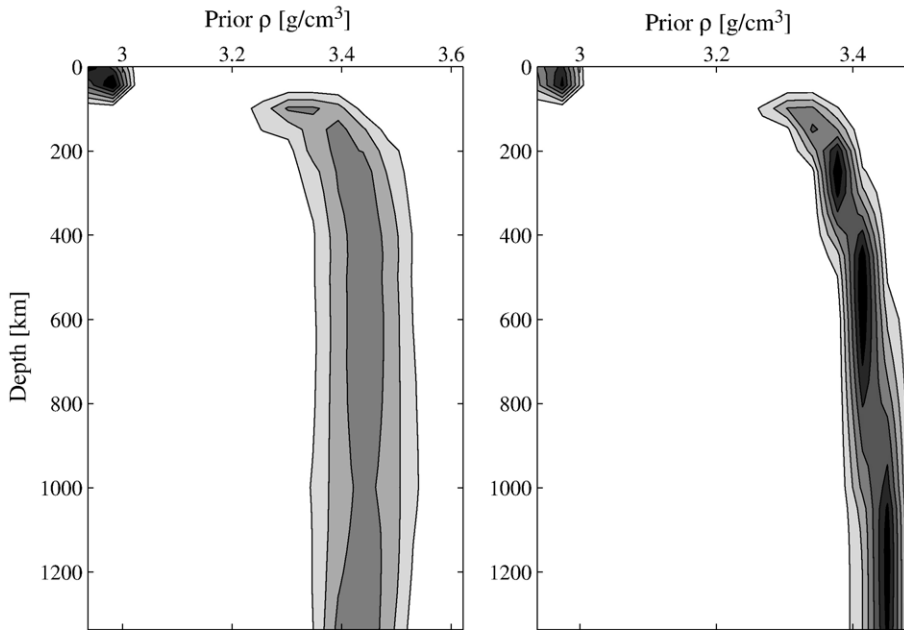


Fig. 8. Marginal prior (left panel) and posterior (right panel) *pdf*'s depicting the mantle density structure as a function of depth for all sampled models. A clear narrowing of the posterior distribution is evident, indicating the significant contribution provided by data. Shades of gray as in Fig. 6.

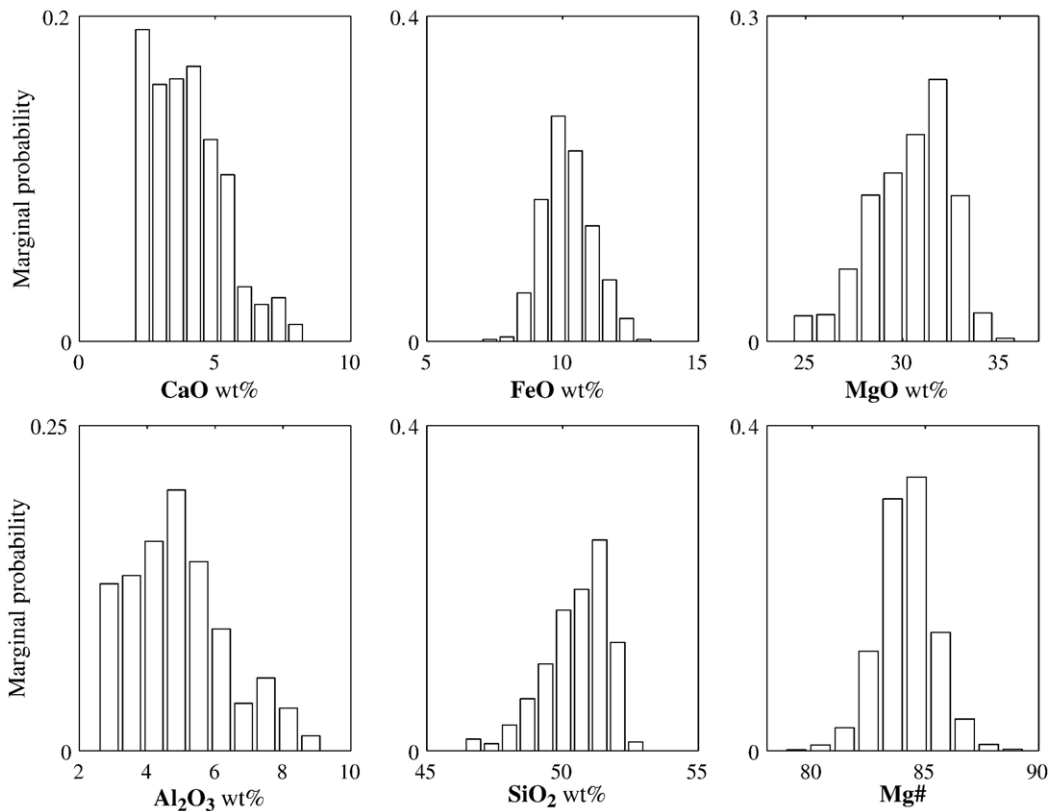


Fig. 9. Marginal posterior *pdf*'s displaying sampled bulk lunar compositions and *Mg#*s for the silicate part of the Moon (crust and mantle).

condition at a depth of 1000 km, in accord with seismic evidence for a rigid lunar mantle (for discussions of these and other geophysical evidence on mantle thermal evolution and present-day state the reader is referred to e.g. [70,73]).

### 8.3. Mantle mineralogy and physical properties

Mineral phases and derived bulk physical properties, in the form of density and conductivity profiles are shown in Figs. 6–8. Again, when compared to previous investigations of lunar electrical conductivity structure, our results are in overall agreement. As already noted, previous investigations found conductivity to increase from  $10^{-4}$ – $10^{-3}$  S/m at a few hundred km depth to roughly  $10^{-2}$ – $10^{-1}$  S/m at about 1100 km depth (e.g. [17]). Lunar density profiles have only been constrained by indirect means, such as mass and moment of inertia considerations [66] as well as in combination with the

constraints provided by derived seismic  $P$  and  $S$ -wave velocity profiles (e.g. [71,72,57]). Although model dependent Kuskov et al. [57] obtained the following density ranges for the mantle 3.22–3.34 g/cm<sup>3</sup> (60–300 km depth), 3.29–3.44 g/cm<sup>3</sup> (300–500 km depth) and 3.34–3.52 g/cm<sup>3</sup> (500 km-core mantle boundary), which are generally in accordance with the mantle densities obtained here.

### 8.4. Bulk composition and Mg#

Bulk sampled compositions and Mg#s for the silicate part of the Moon, i.e. crust and mantle, are displayed in the histograms in Fig. 9. In support of our results, we observe that independent inversion of the Apollo lunar seismic data [73] yields bulk lunar compositions (Fig. 10) that are largely consistent with those obtained here.

A certain care, of course, has to be exercised when drawing inferences from this sort of modeling, involving

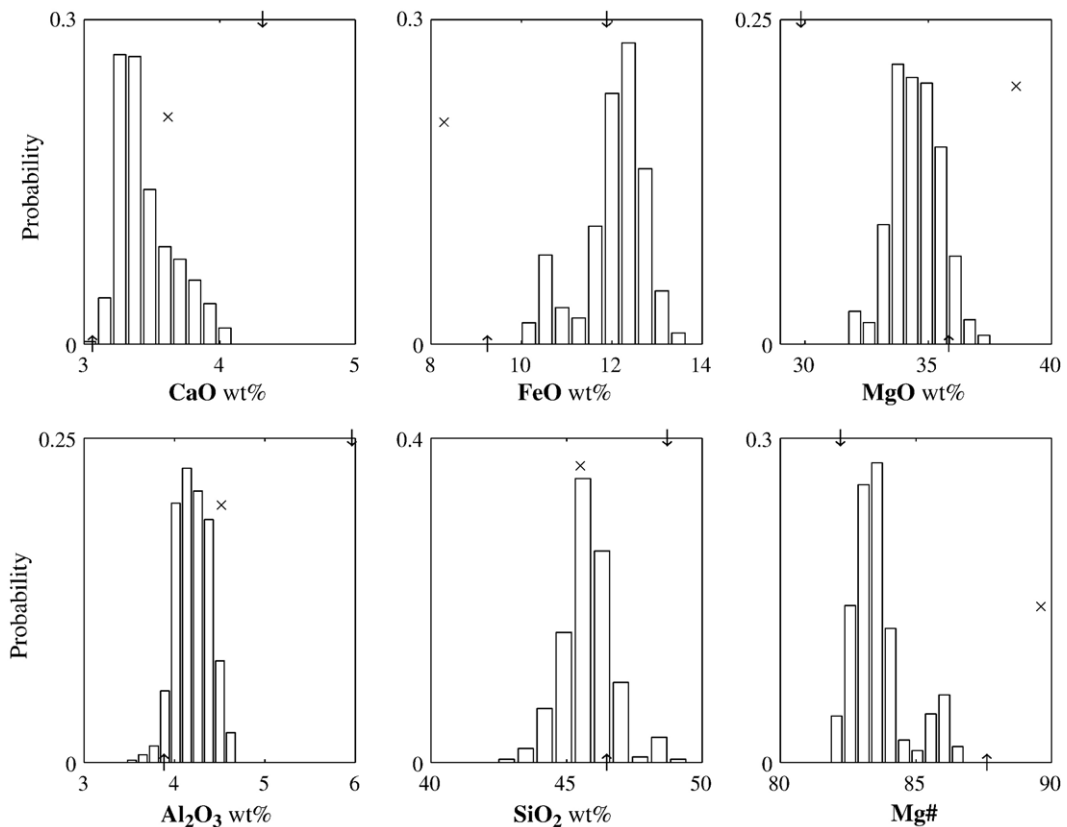


Fig. 10. Marginal posterior  $pdf$ 's showing sampled bulk lunar compositions and Mg#s for the silicate part of the Moon, obtained from an inversion of the Apollo lunar seismic data in combination with mass and moment of inertia [73,74]. The obtained distributions are seen to be in overall agreement with the results presented here (Fig. 9). Upward and downward pointing arrows indicate for comparison bulk compositional estimates derived by Warren [75] and Kuskov and Kronrod [72] (model II), respectively, while crosses denote bulk composition of the Earth's upper mantle estimated by McDonough and Sun [76].

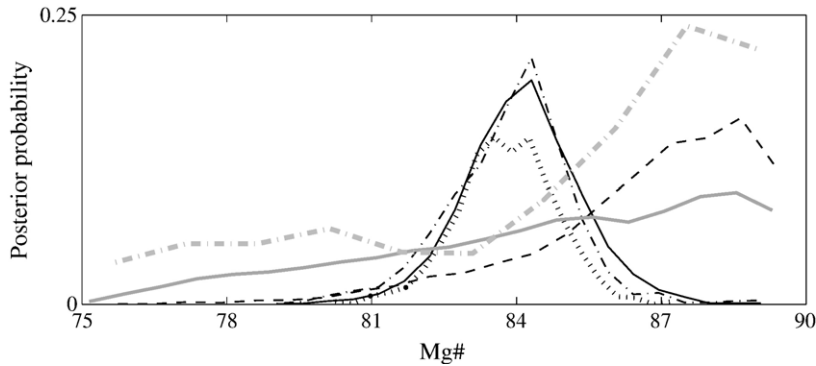


Fig. 11. Marginal prior and several posterior *pdf*'s showing sampled bulk lunar Mg#s for the silicate part of the Moon, obtained from an inversion of prior information (gray line), only gravity data (dashed line), only electromagnetic data (heavy gray dot-dashed line), all data jointly (full line), all data jointly with different random seeds (dotted and dot-dashed line), respectively. The figure clearly shows convergence and stationary of obtained results (see the main text for further explanation), as the parameter values over the three independent chains are similar. Resolution is inferred from comparison of results obtained from sampling prior, individual data sets and full posterior, which reveal that electromagnetic sounding data are more sensitive to composition than gravity data. While we have here considered compositional parameters in exemplifying issues of convergence and resolution, this could equally well have been done using thermal parameters or any other parameters for that matter.

a somewhat uncertain data base. However, the fact that inversion of a different geophysical data set, which senses only elastic properties, results in estimates in overall agreement with what is obtained here is indeed a positive outcome.

### 8.5. Convergence and resolution

Questions regarding convergence and resolution are very important issues when having to draw conclusions from inverse calculations. Criteria usually adopted in investigating the former, and providing adequate confidence in the results, include the necessity of stabilisation of inverted parameter values and similarity of these across independent chains, i.e. runs. Questions regarding the data resolution have already been addressed through the obvious distinction between prior and posterior *pdf*'s displayed here. To provide further insight into how much information is actually contained in the individual data sets, we also inverted these separately. Fig. 11 below summarises the results, in the form of sampled bulk Mg#s, for separate inversions of (1) prior information, (2) only electromagnetic sounding data, (3) only gravity data, and (4) joint inversion of all data using, including results from two independent chains (using different random number sequences). Sampled bulk Mg#s from the three independent posterior chains vary in detail, but their overall characteristics are similar. As concerns inversion of individual data sets, we observe that while the characteristics are different to the full posterior *pdf*, a significant narrowing of the prior *pdf* is nonetheless obtained, thus signaling that individual

data sets are able to provide information on the system.

## 9. Discussion and conclusion

As mentioned in the introduction the purpose of the present study is twofold—(1) to present a novel way of analysing electromagnetic sounding data with the purpose of constraining composition and thermal state of a planet, here exemplified for the Moon, and (2) the integration of widely different geophysical data sets into a joint inversion providing tighter constraints on the internal structure. This is accomplished by appealing to a set of parameters that are common to all the different geophysical fields considered. The obvious advantage here in comparison to traditional inversions stems from the fact that electromagnetic sounding data and gravity data are not a priori linked if described by the physical properties to which they give rise, i.e.  $\sigma$  and  $\rho$ , unless of course appeal is made to measurements or empirical relationships correlating these parameters. Employing composition and temperature thus provides the natural link, in that given these parameters all other properties can be determined. This particular strategy of inverting geophysical data directly for compositional and thermal parameters has already been applied in an inversion of seismic arrival times [74].

We have also shown the sensitivity of electrical conductivity to probing planetary composition by considering a  $\sigma$ - $x$  relationship, in addition to the well-established  $\sigma$ - $T$  relationship. As to the soundness of the results obtained here, the fact that these generally agree

with electrical conductivity and thermal profiles derived earlier, provides some confidence in the overall correctness of what has been undertaken here. Also, in support of our results, we observed that independent inversion of the Apollo lunar seismic data [73,74], yields bulk lunar compositions that are largely consistent with those presented here. However, as the results are directly influenced by the available laboratory electrical conductivity data, it has to be stressed, that well-constrained laboratory measurements of relevant phases are necessary in order to carefully characterise the contributions made by individual phases to the bulk electrical conductivity profile. It is accordingly our hope that future laboratory electrical conductivity measurements will not only include more relevant minerals, such as pyrope and almandine, but will, given that electrical conductivity varies significantly as a function of the composition of individual minerals, also include measurements of systematics.

In summary, the approach presented here of jointly inverting electromagnetic sounding and gravity data to constrain composition and thermal state is feasible and its advantage consists in confronting compositional and thermal parameters directly with geophysical observations and as such is a step beyond the traditional geophysical sequence of first performing field measurements followed by interpretations based on laboratory results.

### Acknowledgements

The authors would like to thank three anonymous reviewers for comments that improved the manuscript. A. Khan gratefully acknowledges financial support from the Carlsberg Foundation.

### References

- [1] M.N. Toksijz, S.C. Solomon, Thermal history and evolution of the moon, *Moon* 7 (1973) 251.
- [2] G. Schubert, R.E. Young, P. Cassen, Subsolidus convection models of the lunar internal temperature, *Philos. Trans. R. Soc. Lond., A* 285 (1977) 523.
- [3] M.N. Toksijz, A.T. Hsui, D.H. Johnston, Thermal evolutions of the terrestrial planets, *Moon Planets* 18 (1978) 281.
- [4] A.B. Binder, M. Lange, On the thermal history, thermal state, and related tectonism of a Moon of fission origin, *J. Geophys. Res.* 85 (1980) 3194.
- [5] T. Spohn, W. Konrad, D. Breuer, R. Zieth, The longevity of lunar volcanism: implications of thermal evolution calculations with 2D and 3D mantle convection models, *Icarus* 149 (2000) 54.
- [6] M.G. Langseth, S.J. Keihm, K. Peters, Revised lunar heat-flow values, in: *Proc. Lunar Planet. Sci. Conf.* 7th, 1976, p. 3143.
- [7] Y. Nakamura, J. Koyama, Seismic Q of the lunar upper mantle, *J. Geophys. Res.* 87 (1982) 4855.
- [8] S. Pullan, K. Lambeck, On constraining lunar mantle temperatures from gravity data, in: *Proc. Lunar Planet. Sci. Conf.* 11th, 1980, p. 2031.
- [9] C.P. Sonett, B.F. Smith, D.S. Colburn, G. Schunbert, K. Schwartz, The induced magnetic field of the moon: conductivity profiles and inferred temperature, in: *Proc. Lunar Planet. Sci. Conf.* 3rd, 1972, p. 2309.
- [10] P. Dyal, C.W. Parkin, W.D. Daily, Structure of the lunar interior from magnetic field measurements, in: *Proc. Lunar Planet. Sci. Conf.* 7th, 1976, p. 3077.
- [11] M.J. Wiskerchen, C.P. Sonett, A lunar metal core? in: *Proc. Lunar Planet. Sci. Conf.* 8th, 1977, p. 515.
- [12] L.L. Hood, F. Herbert, C.P. Sonett, The deep lunar electrical conductivity profile: structural and thermal inferences, *J. Geophys. Res.* 87 (1982) 5311.
- [13] C.P. Sonett, A. Duba, Lunar temperature and global heat flux from laboratory electrical conductivity and lunar magnetometer data, *Nature* 258 (1975) 118.
- [14] A. Duba, H.C. Heard, R.N. Schock, Electrical conductivity of orthopyroxene to 1400 °C and the resulting selenotherm, in: *Proc. Lunar Planet. Sci. Conf.* 7th, 1976, p. 3173.
- [15] J.S. Huebner, L.B. Wiggins, A. Duba, Electrical conductivity of pyroxene which contains trivalent cations—laboratory measurements and the lunar temperature profile, *J. Geophys. Res.* 84 (1979) 4652.
- [16] L.L. Hood, F. Herbert, C.P. Sonett, Further efforts to limit lunar internal temperatures from electrical conductivity determinations, *J. Geophys. Res.* 87 (1982) A109 (Suppl.).
- [17] L.L. Hood, C.P. Sonett, Limits on the lunar temperature profile, *Geophys. Res. Lett.* 9 (1982) 37.
- [18] T.J. Shankland, A. Duba, Standard electrical conductivity of isotropic, homogeneous olivine in the temperature range 1200–1500 °C, *Geophys. J. Int.* 103 (1990) 25.
- [19] A. Kavner, L. Xiaoyuan, R. Jeanloz, Electrical conductivity of a natural (Mg, Fe)SiO<sub>3</sub> majorite garnet, *Geophys. Res. Lett.* 22 (1995) 3103.
- [20] Y. Xu, T.J. Shankland, Electrical conductivity of orthopyroxene and its high pressure phases, *Geophys. Res. Lett.* 26 (1999) 2645.
- [21] Y. Xu, T.J. Shankland, A. Duba, Pressure effect on electrical conductivity of mantle olivine, *Phys. Earth Planet. Inter.* 118 (2000) 149.
- [22] Y. Xu, T.J. Shankland, B.T. Poe, Laboratory-based electrical conductivity in the Earth's mantle, *J. Geophys. Res.* 108 (2000) 2314.
- [23] J. Ducruix, V. Courtillot, J. Le Mouel, The late 1960's secular variation impulse, the eleven year magnetic variation, and the electrical conductivity of the deep mantle, *Geophys. J. R. Astron. Soc.* 61 (1980) 73.
- [24] S.C. Constable, Constraints on mantle electrical conductivity from field and laboratory measurements, *J. Geomagn. Geoelectr.* 45 (1993) 707.
- [25] N. Olsen, The electrical conductivity of the mantle beneath Europe derived from C-responses from 3 to 720 hr, *Geophys. J. Int.* 133 (1998) 298.
- [26] A. Tarantola, B. Valette, Inverse problems: quest for information, *J. Geophys.* 50 (1982) 159.
- [27] A. Tarantola, *Inverse Problem Theory and Model Parameter Estimation*, SIAM, Philadelphia, USA, 2004.
- [28] K. Mosegaard, A. Tarantola, Monte Carlo sampling of solutions to inverse problems, *J. Geophys. Res.* 100 (1995) 12431.

- [29] K. Mosegaard, Resolution analysis of general inverse problems through inverse Monte Carlo sampling, *Inverse Probl.* 14 (1998) 405.
- [30] K. Mosegaard, M. Sambridge, Monte Carlo analysis of inverse problems, *Inverse Probl.* 18 (2002) 29.
- [31] R.J. Phillips, The lunar conductivity profile and the nonuniqueness of electromagnetic data inversion, *Icarus* 17 (1972) 88.
- [32] B.A. Hobbs, The inverse problem of the moon's electrical conductivity, *Earth Planet. Sci. Lett.* 17 (1973) 380.
- [33] B.A. Hobbs, The electrical conductivity of the moon: an application of inverse theory, *Geophys. J. R. Astron. Soc.* 51 (1977) 727.
- [34] B.A. Hobbs, L.L. Hood, F. Herbert, C.P. Sonett, An upper bound on the radius of a highly electrically conducting lunar core, *J. Geophys. Res.* 88 (1983) B97 (Suppl.).
- [35] C.P. Sonett, Electromagnetic induction in the moon, *Rev. Geophys. Space Phys.* 20 (1982) 411.
- [36] L.L. Hood, Geophysical constraints on the interior of the Moon, in: W.K. Hartmann, R.J. Phillips, G.J. Taylor (Eds.), *Origin of the Moon*, LPI, Houston, 1986, p. 361.
- [37] A.E. Ringwood, E. Essene, Petrogenesis of the Apollo 11 basalts, internal constitution and origin of the Moon, in: *Proc. Apollo 11 Lunar Sci. Conf.*, 1, 1970, p. 769.
- [38] A. Duba, M. Dennison, A.J. Irving, C.R. Thornber, J.S. Huebner, Electrical conductivity of aluminous orthopyroxene, *Lunar Planet. Sci. X*, Abstract, 1979, p. 318.
- [39] S.R. Taylor, *Planetary Science: A Lunar Perspective*, LPI, Houston, 1982.
- [40] M.A. Wieczorek, M.T. Zuber, The composition and origin of the lunar crust: constraints from central peaks and crustal thickness modeling, *Geophys. Res. Lett.* 28 (2001) 4023.
- [41] P.H. Warren, The magma ocean concept and lunar evolution, *Annu. Rev. Earth Planet. Sci.* 13 (1985) 201.
- [42] S.E. Kesson, A.E. Ringwood, Mare basalt petrogenesis in a dynamic moon, *Earth Planet. Sci. Lett.* 30 (1976) 155.
- [43] Y. Nakamura, Farside deep moonquakes and deep interior of the Moon, *J. Geophys. Res.* 110 (E1) (2005), doi:10.1029/2004JE002332.
- [44] A. Khan, K. Mosegaard, An inquiry into the lunar interior: a non-linear inversion of the Apollo lunar seismic data, *J. Geophys. Res.* 107 (E6) (2002), doi:10.1029/2001JE001658.
- [45] P. Lognonné, J. Gagnepain-Beyneix, H. Chenet, A new seismic model of the Moon: implications for structure, thermal evolution and formation of the Moon, *Earth Planet. Sci. Lett.* 211 (2003) 27.
- [46] A. Duba, Are laboratory electrical conductivity data relevant to the Earth? *Acta Geod. Geophys. Montan. Acad. Sci. Hung. Tomus* 11 (1976) 485.
- [47] S.C. Constable, A. Duba, The electrical conductivity of olivine, a dunite, and the mantle, *J. Geophys. Res.* 95 (1990) 6967.
- [48] A. Duba, J.N. Boland, A.E. Ringwood, The electrical conductivity of pyroxene, *J. Geol.* 81 (1973) 727.
- [49] J.A. Tyburczy, D.K. Fisler, Electrical properties of minerals and melts, in: T.J. Ahrens (Ed.), *Mineral Physics and Crystallography: A Handbook of Physical Constants*, AGU, Washington, DC, 1995, p. 185.
- [50] A. Duba, H.C. Heard, R.N. Schock, Electrical conductivity of olivine at high pressure and under controlled oxygen fugacity, *J. Geophys. Res.* 79 (1974) 1667.
- [51] M. Sato, Oxygen fugacity and other thermochemical parameters of Apollo 17 high-Ti basalts, in: *Proc. Lunar Planet. Sci. Conf.* 7th, 1976, p. 1323.
- [52] J.W. Delano, Redox state of the Moon's interior, Oxygen in the Terrestrial Planets, Abstract# 3008, LPI, Houston, 2004.
- [53] L.T. Elkins, V.A. Fernandez, W.W. Delano, T.L. Grove, Origin of lunar ultramafic green glasses: constraints from phase equilibrium studies, *Geochim. Cosmochim. Acta* 64 (2000) 2339.
- [54] Y. Nakamura, D. Lammlein, G.V. Latham, M. Ewing, J. Dorman, F. Press, M.N. Toksöz, New seismic data on the state of the deep lunar interior, *Science* 181 (1973) 49.
- [55] N. Metropolis, A.W. Rosenbluth, M.N. Rosenbluth, A.H. Teller, E. Teller, Equation of state calculations by fast computing machines, *J. Chem. Phys.* 21 (1955) 1087.
- [56] W.K. Hastings, Monte Carlo sampling methods using Markov chains and their applications, *Biometrika* 57 (1973) 97.
- [57] O.L. Kuskov, V.A. Kronrod, L.L. Hood, Geochemical constraints on the seismic properties of the lunar mantle, *Phys. Earth Planet. Inter.* 134 (2002) 175.
- [58] D.P. Dobson, J.P. Brodholt, The electrical conductivity and thermal profile of the Earth's mid-mantle, *Geophys. Res. Lett.* 27 (2000) 2325.
- [59] J.A.D. Connolly, Computation of phase equilibria by linear programming: a tool for geodynamic modeling and an application to subduction zone decarbonation, *Earth Planet. Sci. Lett.* 236 (2005) 524.
- [60] T.J.B. Holland, R. Powell, An internally consistent thermodynamic data set for phases of petrological interest, *J. Metamorph. Geol.* 16 (1998) 309.
- [61] B.J. Wood, J.R. Holloway, A thermodynamic model for subsolidus equilibria in the system CaO–MgO–Al<sub>2</sub>O<sub>3</sub>–SiO<sub>2</sub>, *Geochim. Cosmochim. Acta* 66 (1984) 159.
- [62] J.G. Berryman, Mixture theories for rock properties, in: T.J. Ahrens (Ed.), *American Geophysical Union Handbook of Physical Constants*, AGU, Washington, DC, 1995, p. 205.
- [63] U. Schmucker, *Magnetic and electric fields due to electromagnetic induction by external sources*, Landolt-Bornstein, New Series, 5/2b, Springer-Verlag, Berlin, 1985, p. 100.
- [64] W.D. Parkinson, V.R.S. Hutton, The electrical conductivity of the Earth, in: J.A. Jacobs (Ed.), *Geomagnetism*, vol. 3, Academic Press, London, 1989, p. 261.
- [65] M.A. Wieczorek, B.L. Jolliff, J.J. Gillis, L.L. Hood, K. Righter, A. Khan, M.E. Pritchard, B.P. Weiss, S. Thompkins, J.G. Williams, The constitution and structure of the lunar interior, in *New Views of the Moon*, in press.
- [66] A. Konopliv, A.B. Binder, L.L. Hood, A.B. Kucinskis, W.L. Sjögren, J.G. Williams, Improved gravity field of the moon from lunar prospector, *Science* 281 (1998) 1476.
- [67] M. Hirschmann, Mantle solidus: experimental constraints and the effects of peridotite composition, *Geochem. Geophys. Geosyst.* 1 (2000), doi:10.1029/2000GC000070.
- [68] B.L. Jolliff, J.J. Gillis, L.A. Haskin, R.L. Korotev, M.A. Wieczorek, Major crustal terranes: surface expressions and crust–mantle origins, *J. Geophys. Res.* 105 (2000) 4197.
- [69] F. Herbert, L.D. Smith, L.L. Hood, C.P. Sonett, Waves in the Earth's magnetosheath, the high frequency electromagnetic response of the Moon and the shallow (150–250 km depth) lunar electrical conductivity profile, *Lunar Planet. Sci.* XIII (1982) 321.
- [70] M.E. Pritchard, D.J. Stevenson, Thermal aspects of a lunar origin by giant impact, in: R.M. Canup, K. Righter (Eds.), *Origin of the Earth and Moon*, Arizona University Press, Arizona, 2000, p. 179.

- [71] L.L. Hood, J.H. Jones, Geophysical constraints on lunar bulk composition and structure: a reassessment, *J. Geophys. Res.* 92 (1987) 396.
- [72] O.L. Kuskov, V.A. Kronrod, Constitution of the Moon: 5. Constraints on density, temperature and radius of a core, *Phys. Earth Planet. Inter.* 107 (1998) 285.
- [73] A. Khan, J. Maclennan, S.R. Taylor, J.A.D. Connolly, Are the Earth and the Moon compositionally alike?-Inferences on lunar composition and implications for lunar origin and evolution from geophysical modeling, *J. Geophys. Res.* 111 (2006) E05005, doi:10.1029/2005JE002608.
- [74] A. Khan, J.A.D. Connolly, J. Maclennan, K. Mosegaard, Joint inversion of gravity and seismic data for lunar composition and thermal state, *Geophys. J. Int.* (in press).
- [75] P.H. Warren, “New” lunar meteorites: II. Implications for composition of the global lunar surface, lunar crust, and the bulk Moon, *Meteorit. Planet. Sci.* 40 (2005) 1.
- [76] W.F. McDonough, S.S. Sun, The composition of the Earth, *Chem. Geol.* 120 (3–4) (1995) 223.